Preprint typeset using LaTeX style emulateapj v. 11/12/01

THE BOSTON UNIVERSITY–FIVE COLLEGE RADIO ASTRONOMY OBSERVATORY GALACTIC RING SURVEY

J. M. Jackson, J. M. Rathborne, R. Y. Shah, R. Simon[1], T. M. Bania, D. P. Clemens, E. T. Chambers, A. M. Johnson, M. Dormody, R. Lavoie
Institute for Astrophysical Research, Boston University, 725 Commonwealth Avenue, Boston, MA 02215; jackson@bu.edu, rathborn@bu.edu, ronak@bu.edu, simonr@ph1.uni-koeln.de, bania@bu.edu, clemens@bu.edu, etc1@bu.edu, alexj@bu.edu, mdormody@bu.edu, coldfury@bu.edu
AND
M. H. Heyer
Department of Astronomy, Lederle Graduate Research Tower, University of Massachusetts, Amherst, MA 01003; heyer@astro.umass.edu

ABSTRACT

The Boston University-Five College Radio Astronomy Observatory Galactic Ring Survey is a new survey of Galactic ^{13}CO $J = 1 \rightarrow 0$ emission. The survey used the SEQUOIA multi pixel array on the Five College Radio Astronomy Observatory 14 m telescope to cover a longitude range of $\ell = 18°$–$55.7°$ and a latitude range of $|b| < 1°$, a total of 75.4 square degrees. Using both position-switching and On-The-Fly mapping modes, we achieved an angular sampling of $22''$, better than half of the telescope's $46''$ angular resolution. The survey's velocity coverage is -5 to 135 km s^{-1} for Galactic longitudes $\ell \leq 40°$ and -5 to 85 km s^{-1} for Galactic longitudes $\ell > 40°$. At the velocity resolution of 0.21 km s^{-1}, the typical rms sensitivity is $\sigma(T_A^*) \sim 0.13$ K. The survey comprises a total of 1,993,522 spectra. We show integrated intensity images (zeroth moment maps), channel maps, position-velocity diagrams, and an average spectrum of the completed survey dataset. We also discuss the telescope and instrumental parameters, the observing modes, the data reduction processes, and the emission and noise characteristics of the dataset. The Galactic Ring Survey data are available to the community at www.bu.edu/galacticring or in DVD form by request.

Subject headings: surveys–ISM: clouds–ISM: molecules–Galaxy: kinematics and dynamics–radio lines: general

1. INTRODUCTION

The Galactic distribution of molecular hydrogen was first deduced from early CO observations (Burton et al. 1975; Scoville & Solomon 1975). Surprisingly, the CO had a Galactocentric radial distribution distinct from that of atomic hydrogen. In particular, the CO distribution in the northern hemisphere showed a large peak in the molecular gas density about midway between the Sun and the Galactic Center. Subsequent determinations of the face-on distribution of CO showed that this feature, dubbed the "5 kpc ring," dominates the Galaxy's molecular gas structure (Clemens et al. 1988).

Most of the Galaxy's star formation activity takes place in the 5 kpc ring. With a mass of $2{\times}10^9$ M$_\odot$, the 5 kpc ring contains about 70% of all of the molecular gas inside the solar circle (Clemens et al. 1988). The ring is thus an enormous reservoir of material for the formation of new stars and clusters. Indeed, most of the Galactic giant H II regions, far infrared luminosity, diffuse ionized gas, and supernova remnants are associated with the ring (Burton 1976; Robinson et al. 1984).

Because the 5 kpc ring dominates both the molecular interstellar medium (ISM) and the star formation activity in the Milky Way, it plays a crucial role in the dynamics, structure, and chemical evolution of our Galaxy. Yet, despite its obvious importance, the 5 kpc ring has remained poorly understood, mostly due to the challenge of imaging such a large expanse of sky (several tens of square degrees) at good angular resolution and sensitivity.

Recent advances in millimeter-wave array technology now allow a comprehensive study of molecular gas in the 5 kpc ring. In particular, the development of monolithic microwave integrated circuits (MMICs) has enabled the construction of large focal plane array receivers at millimeter wavelengths and a corresponding improvement in mapping speed. Using such an array, we have conducted a new ^{13}CO $J = 1 \rightarrow 0$ molecular line survey of the inner Galaxy, the Boston University-Five College Radio Astronomy Observatory Galactic Ring Survey (GRS).

Although many previous surveys mapped the Galaxy in the main isotopic ^{12}CO $J = 1 \rightarrow 0$ transition, we have chosen to conduct the GRS in the ^{13}CO $J = 1 \rightarrow 0$ transition. Because ^{13}CO is much less abundant than ^{12}CO, the ^{13}CO transition has a smaller optical depth. It is therefore a better column density tracer than ^{12}CO. Moreover, the smaller optical depths result in narrower linewidths for ^{13}CO, and consequently, blended lines from two distinct clouds at similar velocities can be separated more cleanly.

In this paper, we describe the survey, the data reduction procedures, and the emission and noise characteristics of the dataset. Analyses of the survey will be published in future papers.

2. THE SURVEY

[1] Present address, I.Physikalisches Institut, Universität zu Köln, Zülpicher Strasse 77, 50937 Köln, Germany.

2.1. *Telescope, Receiver, and Backend Parameters*

The GRS was conducted using the Five College Radio Astronomy Observatory (FCRAO) 14 m telescope located in New Salem, Massachusetts between 1998 December and 2005 March. The survey covers the region between $18^\circ < \ell < 55.7^\circ$ and $|b| < 1^\circ$. At the ^{13}CO $J = 1 \rightarrow 0$ frequency ($\nu_0 = 110.2$ GHz), the beam-width of the FCRAO 14 m is $46''$.

All observations were obtained using the single sideband focal plane array receiver SEQUOIA (SEcond QUabbin Optical Imaging Array; Erickson et al. 1999). SEQUOIA employs low-noise MMIC based amplifiers. Before 1999, the MMICs were InP which provided a mean receiver noise temperature of 80 K. After 1999, SEQUOIA was upgraded to InSb MMICs which provided a mean receiver noise temperature of 60 K.

For the observing period 1998–2001, SEQUOIA contained 16 separate receiving elements. These elements were arranged in a singly-polarized 4×4 array with a separation between elements of $88''$ on the sky. In this observing period, SEQUOIA was used in combination with a spectrometer consisting of 16 autocorrelators. Each autocorrelator had a bandwidth of 40 MHz, 512 channels, and a velocity sampling of 0.21 km s^{-1}. The autocorrelators were centered at a velocity of 40 km s^{-1} and thus covered the velocity range -10 to 90 km s^{-1}. This setup was sufficient to cover the local standard of rest (LSR) velocities[2] for most of the ^{13}CO emission for Galactic longitudes $\ell > 40^\circ$.

In 2002 January, a new autocorrelator, the dual channel correlator (DCC), was commissioned. The DCC enabled the processing of two independent intermediate frequencies (IFs). The DCC was configured to have a bandwidth of 50 MHz, 1024 channels, and a velocity sampling of 0.13 km s^{-1} for both of the IFs. In order to provide enough velocity coverage to sample all Galactic ^{13}CO emission below Galactic longitudes of 40°, the two IFs were both tuned to the ^{13}CO transition but centered separately at LSR velocities of 20 km s^{-1} and 100 km s^{-1}. This setup provided 270 channels of overlap between the IFs and thus allowed us to generate a composite spectrum for each position on the sky with a total of 210 km s^{-1} bandwidth. In 2002 March, SEQUOIA was upgraded from a 16 element array to a 32 element dual-polarization array with two IFs for each of the 32 detector elements. The combination of the upgraded SEQUOIA and the DCC enabled processing of both IFs for each of the 32 pixels, resulting in 64 simultaneously observed spectra.

2.2. *Pointing Checks*

Pointing checks were conducted at the beginning of every observing session (typically lasting a total of eight hours) using the SiO masers T Ceph or χ Cyg. When the observing session extended beyond sunrise (April–May), additional pointing checks were also performed using the SiO maser R Cas.

The pointing offsets were determined using a five-point pattern and were adjusted iteratively to find the optimum pointing of the telescope. When the fits to the pointing correction coverged to $\leq 5''$ no more pointing corrections were adopted. At this point, the focus was then adjusted and a parabolic fit to the resultant intensities determined the optimal focus. Once the optimal focus was achieved, the five-point pointing procedure was repeated. We therefore estimate that the pointing accuracy is better than $5''$.

2.3. *Selection of Emission-Free Sky Positions*

To account for millimeter wave emission from the sky, it is necessary to subtract the sky emission from a nearby "off" position from the spectrum of the source position. Because the Galactic plane contains extended, strong ^{13}CO emission, we had to choose "off" positions carefully to avoid contaminating the source position with unwanted emission in the "off" position.

To select "off" positions with little or no ^{13}CO emission, we examined ^{12}CO maps from the Columbia/CfA survey in order to find positions as close as possible to the Galactic plane with little or no emission (T. M. Dame 1998, private communication). We then searched these potential emission-free positions in ^{13}CO by position-switched observations against regions from the Columbia/CfA survey known to be free of emission in ^{12}CO to an rms noise level of 0.05 K (for 0.65 km s^{-1} velocity resolution). For all but one position, no ^{13}CO emission was found toward the sky positions above a noise level of T_{mb}=0.07 K. One of the "off" positions, however, possesses a narrow ^{13}CO emission feature $T_A^* \sim 0.1$ K at V_{LSR}=15 km s^{-1}, affecting data in the range ℓ=32.°5 to 36° and b=−0.5 to 0.°8. This contamination manifests itself as a negative spectral artifact feature in the final dataset. In total fifty-two "off" positions were used for the GRS. For each map we selected the nearest possible "off" position, which was typically $< 2^\circ$ from the source position in both Galactic longitude and latitude.

2.4. *Observing Modes*

The majority of the observations were conducted remotely. Due to weather constraints, the observing season was typically limited to the months of November through May. From the FCRAO, the lowest Galactic longitude covered by the GRS reached a maximum elevation of about 45°. To avoid observations at high air mass, all GRS data were obtained at elevations >29°. To maintain uniform data quality, we did not observe if the system temperature exceeded 400 K. The typical system noise temperatures were 200–300 K.

We employed three separate observing modes to map the Galactic ^{13}CO $J = 1 \rightarrow 0$ emission: position-switching with the 16-element SEQUOIA (1998 December–2001 May), On-The-Fly (OTF) mapping with the 16-element SEQUOIA (2002 Jan–March), and OTF mapping with the upgraded 32-element SEQUOIA (2002 March–2005 March).

In the position-switching mode, the data were obtained by stepping the array $22.''14$ in a 16×16 grid (these grids were referred to as "footprint"). In this mode the dewar containing the focal plane array receiver was rotated continuously to align the array in Galactic coordinates. This scheme produced a fully sampled "footprint" map with a

[2] To deduce our LSR velocity scale we used the IAU J2000 standards for the solar motion with respect to the LSR of $\alpha = 271^\circ$ and δ=30°. For consistency with previous FCRAO observations we use $V_\odot$=20 km s^{-1} rather than the IAU standard of $V_\odot$=19.4 km s^{-1}.

size of $\ell \times b = 5\farcm9 \times 5\farcm9$. Four consecutive array pointings shared the same emission-free "off" position. Integration times per point for one on-source pointing ranged between 10 and 20 s, with 20 to 40 s spent on the emission-free "off" position. Most positions were observed twice to achieve the desired sensitivity. The resulting spectra have an average 1 σ rms noise level $T_A^* = 0.20$ K per 0.21 km s^{-1} channel. In a typical eight-hour observing session, we covered ~ 0.35 deg^2. Due to the limitations in the velocity coverage of the autocorrelators, the observations during this period were restricted to Galactic longitudes >40°, where the velocity of the Galactic ^{13}CO emission is always <85 km s^{-1}. In the 2.5 years using this mode, we mapped the region from $\ell = 40°$ to 51° and $b = -1°$ to 0.5° (16 deg^2; 21.2% of the entire survey).

In 2002 January, the OTF mapping mode was implemented on the FCRAO. In this mode, the telescope is scanned across the sky and data are collected as the telescope moves. Because the data storage, slew, and settling times are greatly reduced, data obtained in this mode have far less overhead and are consequently more efficiently collected. Since in the OTF mode the SEQUOIA dewar does not rotate to compensate for the field rotation, the mapped region is covered on a highly irregular, yet very densely-sampled grid. This has several consequences. In the central region of the OTF map, every pixel is scanned over every position in the map. Compared to the position-switching mode, this redundancy enhances the data quality since pixel-to-pixel variations are averaged. Artifacts due to gain and noise variations among pixels, therefore, are greatly reduced. Towards the map edges, the coverage becomes less dense. Therefore, the noise is only uniform in the inner, well sampled part of the map and increases towards the map edges. To compensate for this effect and achieve more uniform noise in the final data set, we overlapped many individual maps to cover the survey region. The survey region in OTF mode was broken up into blocks of $\ell \times b = 6' \times 18'$. Each OTF map consisted of a single one of these blocks. For each map, the telescope scanned in Galactic latitude at a rate of 0.35 arcmin s^{-1} in a raster pattern. To sample the emission within the mapping region sufficiently, the array was offset by 0.75 of the beam (35″) between scanning rows. The data were read out at a frequency of 1 Hz as the telescope scanned so that 1 sec integration time was spent on each of the 64 readouts (32 array elements, two velocity settings). We integrated for 10 sec on the emission-free "off" position, after every second row ($\sim$ every 2 mins).

Because we scanned the array during observations, the beam may be slightly elongated for the OTF data. This will only affect the beam in the scanning direction and is estimated to be < 5 % (< 2.″3).

If weather permitted, in an eight-hour observing session we completed $\sim$ 20 OTF maps (~ 0.6 deg^2). Within each observing session, the maps were chosen to span specific ranges in Galactic longitude depending on the local sidereal time, so that we were always obtaining data at high elevations and hence low system temperatures.

In the three months of using the OTF mode with the 16-element SEQUOIA, we surveyed a total solid angle of 5.3 deg^2 (7.0 % of the entire survey). The spectra obtained in this mode have a mean 1 σ rms noise level $T_A^* = 0.18$ K per 0.21 km s^{-1} channel. From March 2002, we used the upgraded 32-element SEQUOIA in the OTF mode. We completed the remainder of the survey region in this mode, $\sim$ 54.1 deg^2 (71.8 % of the entire survey). These spectra have a mean 1 σ rms noise level $T_A^* = 0.13$ K per 0.21 km s^{-1} channel. For a more complete discussion of the noise see § 5.2.

2.5. *Flux Calibration*

The spectra were calibrated using a vane to switch between emission from the sky and an ambient temperature load. The calibration occurred before the start of each map and after every 10 rows during the map ($\sim$ every 10 mins). This method of calibration produces typical errors in the temperature scale of 10–15%.

To verify the system setup and to keep a record of the system performance over the duration of the survey, we obtained a single position-switched observation of W51 at the start of each observing session. An analysis of these data show that the W51 peak brightness temperature showed an rms dispersion of $\sim$ 15%. We use this value as an estimate of the accuracy of our flux scale.

All intensities are reported on the antenna temperature scale, T_A^* (K). To convert antenna temperatures to main-beam brightness temperatures, the T_A^* values should be divided by the main-beam efficiency η_{mb} of 0.48 derived from observations of planets.

2.6. *Data Reduction*

The position-switched raw data were converted to CLASS[3] format. Subsequent analysis was made with the CLASS software package. Each "footprint" was processed individually. To facilitate baseline removal, an average spectrum of each "footprint" was inspected to determine velocity ranges with significant emission to be excluded from the polynomial baseline fit. Together with the order of the baseline fit, these velocity "windows" were altered until a suitable fit was achieved. The polynomial order of the final baseline fit was typically first (linear) or second (parabolic). The velocity windows and the baseline order were then applied to fit spectral baselines for each individual spectrum within the "footprint."

The OTF data were processed at FCRAO with the GUI based program OTFTOOL[4]. We used this program to regrid the irregularly sampled OTF data onto the same 22.″14 grid as the position-switched data. Each raw OTF spectrum was convolved onto a regular grid using a spatial kernel that minimized aliased noise power while retaining the full resolution of the telescope. The kernel is

$$\frac{J_1(2\pi a x)}{2\pi a x}\frac{J_1(cx/R_{max})}{cx/R_{max}}e^{-(2bx)^2}\Pi(R_{max}) \qquad (1)$$

and is similar to kernels used at other telescopes that have implemented OTF mapping (Mangum et al. 2000). J_1 is the first order Bessel function. The variable x is the distance from the observed data point from the output grid cell position in units of λ/D where λ is the observed wavelength of the observation and D is the diameter of the

[3] CLASS is part of the GILDAS package.

[4] OTFTOOL was written by M.H. Heyer, G. Narayanan, and M. Brewer.

FCRAO telescope. R_{max} is the truncation radius of the kernel in units of λ/D, beyond which the kernel is zero. For all regridding of the GRS data, R_{max}= 3. The coefficients, a, b, are determined to minimize the aliased noise power given the edge taper of the FCRAO telescope. The values are a=0.9009, b=0.21505. The coefficient, c=3.831706, corresponds to the first null of $J_1(x)$. The function $\Pi(R_{max})$ acts as a pill box function where Π=1 for R<R_{max} and Π=0 for R>R_{max}.

The resulting spectra for each IF were converted separately and stored in a single CLASS spectral file. The next step in the data reduction process was to combine the spectra from the two IFs. This was achieved by resampling the spectra on a common velocity grid and producing a composite spectrum by merging the spectra for the two IFs. Data from -10 km s^{-1} and 80 km s^{-1} from the first IF were merged with data from 45 km s^{-1} to 140 km s^{-1} from the second IF. For the OTF data, an average spectrum for a $0\overset{\circ}{.}3\times0\overset{\circ}{.}3$ region was used to determine the velocity windows and baseline order (again, typically linear or parabolic), which were then applied to fit spectral baselines for each individual merged spectrum within the region.

The OTF data obtained with the higher velocity resolution (0.13 km s^{-1}) were resampled to 0.21 km s^{-1} to match spectra from the position-switching mode. All spectra were then assembled into 3-dimensional data cubes (ℓ,b,v) using CLASS routines. These cubes were then converted into FITS format using routines within the GILDAS[5] package. Routines written using the CFITSIO libraries were then used to merge the individual FITS cubes into the larger cubes that comprise the final data release.

The final data release contains twenty FITS cubes. Eighteen of these cubes are $\ell \times b = 2^\circ \times 2^\circ$, one is $\ell \times b = 1^\circ \times 2^\circ$, and one is $\ell \times b = 0\overset{\circ}{.}7 \times 2^\circ$. The $2^\circ \times 2^\circ$ data cubes are centered at even integral values of Galactic longitudes from 20° to 54°. The $1^\circ \times 2^\circ$ cube is centered at a Galactic longitude of $18\overset{\circ}{.}5$, and the $0\overset{\circ}{.}7 \times 2^\circ$ cube is centered at a Galactic longitude of $55\overset{\circ}{.}35$. All cubes are centered in Galactic latitude at $b = 0^\circ$. Cubes centered at Galactic longitudes $\leq 40^\circ$ span a velocity range of $V_{LSR} = -5$ to 135 km s^{-1}, while cubes centered at Galactic longitudes $> 40^\circ$ span a velocity range of V_{LSR}=-5 to 85 km s^{-1}(in both cases the data within 5 km s^{-1} from the edge of the passband were discarded). All cubes have identical channel widths of 0.21 km s^{-1}, but a different number of channels depending on whether the center Galactic longitude is $\leq 40^\circ$ (659 channels) or $> 40^\circ$ (424 channels). Although the cube centered at $\ell = 40^\circ$ contains 659 velocity channels, for the region where $40^\circ < \ell < 41^\circ$ the velocity channels above 85 km s^{-1} are blank. The complete survey contains $\sim$ 5 Gbytes of data.

3. COMPARISON TO PREVIOUS CO LINE SURVEYS

The GRS has mapped the Galactic plane in the ^{13}CO $J = 1 \rightarrow 0$ transition. Unlike the optically thick ^{12}CO $J = 1 \rightarrow 0$ transition, which suffers from velocity crowding, the ^{13}CO $J = 1 \rightarrow 0$ transition has a lower optical depth and, therefore, narrower linewidths. ^{13}CO thus allows both a better determination of column density and also a cleaner separation of velocity components. Moreover, because of the improvement in mapping speed allowed by an array receiver, the GRS achieves half-beam sampling. Unlike most previous surveys of molecular emission, the GRS realizes the full resolution of the telescope. Table 1 compares the GRS to the previous CO surveys: the University of Massachusetts-Stony Brook survey (UMSB; Sanders et al. 1986), the Bell Labs Survey (Lee et al. 2001), and the Columbia/CfA survey (Dame et al. 1987).

4. THE DATA

4.1. *Integrated Intensity Image*

Figure 1 shows the integrated intensity image (zeroth moment map) of GRS ^{13}CO emission integrated over all velocities (from V_{LSR}=-5 to 135 km s^{-1} for Galactic longitudes $\ell \leq 40^\circ$ and $V_{LSR} = -5$ to 85 km s^{-1} for Galactic longitudes $\ell > 40^\circ$).

The map was constructed using a masked moment procedure. In this method, the intensity integrated over the specified velocity range towards each position of the map is not simply determined from the sum over all velocity channels. Instead, for any given position (x,y) and velocity channel i, the value $T_i$dv for that position is only included in the sum of the total integrated intensity if two conditions are met: (1) the value of both the central pixel and all 8 neighboring spatial pixels in the same velocity channel exceed the temperature threshold, and (2) the value of the central pixel and the two neighboring velocity pixels in adjacent channels also exceed the temperature threshold. Details of the method are described by Adler et al. (1992). For the GRS data, we used a temperature threshold of T_A^* = 0.6 K.

This image reveals that most of the ^{13}CO molecular line emission is confined near $b \sim 0^\circ$ with concentrations at $\ell \sim 23^\circ$ and $\sim 31^\circ$ (peak integrated intensities of 72 and 68 K km s^{-1} respectively). A large number of distinct clouds can be seen in the integrated intensity image. The brightest of these correspond to well-known star-forming regions such as W51 and W49. A striking aspect of the image is the abundance of filamentary and linear structures and the complex morphology of individual clouds.

4.2. *Channel Maps*

Figure 2 shows channel maps that were made by integrating the ^{13}CO emission over 10 km s^{-1} velocity bins. The channel maps separate emission features along the same line of sight into individual clouds. In addition, individual clouds too faint to be prominent in the integrated intensity image often appear as obvious distinct features in the channel maps.

4.3. *Position-Velocity Diagram*

Figure 3 shows the longitude-velocity (ℓ−v) diagram of the GRS ^{13}CO emission. This diagram was made by averaging the emission over the full coverage in Galactic latitude. To show how the emission varies as a function of Galactic latitude, we have also made (ℓ−v) diagrams over five ranges in latitude in steps of $\Delta b = 0\overset{\circ}{.}4$ (Fig. 4).

[5] The GILDAS working group is a collaborative project of the Observatoire de Grenoble and Institut de Radio Astronomie Millimetrique (IRAM), and comprises: G. Buisson, L. Desbats, G. Duvert, T. Forveille, R. Gras, S. Guilloteau, R. Lucas, and P. Valiron.

These position-velocity diagrams reveal large-scale features, especially the feature commonly called the "molecular ring." We stress that bright regions in the (ℓ−v) diagram arise from a complicated combination of the Galactic column density and the Galaxy's velocity field, and that the "molecular ring" may not represent a real ring-like feature.

4.4. *Integrated Spectrum*

Figure 5 shows the averaged ^{13}CO spectrum for the entire GRS. Every position was averaged together with equal weighting to create this spectrum. The effect is somewhat analogous to observing a portion of an external edge-on galaxy's disk with a single pixel.

The GRS detects ^{13}CO emission at every positive velocity allowed by Galactic rotation. Nevertheless, distinct velocity features can still be recognized, for instance, the peak of the emission occurs at a velocity of about 57 $\mathrm{km\,s^{-1}}$. Whether these velocity features correspond to distinct physical structures or merely result from velocity crowding effets is the subject of future papers.

5. DATA CHARACTERISTICS

5.1. *Emission Characteristics*

Figure 6 plots a histogram of the antenna temperature distribution for all independent (ℓ,b,v) elements ("voxels") in the GRS. The inset shows the same plot but on a linear rather than logarithmic scale. We also show a Gaussian fit to the distribution in the linear scale plot. The fitted Gaussian peaks at 0.014 K and has a full-width at half-maximum of 0.29 K.

Purely random noise would produce a voxel distribution centered exactly at zero with a Gaussian shape. Although a Gaussian fits the data fairly well, there is excess emission, especially in the wings of the distribution. The positive excess reflects the presence of ^{13}CO emission. The negative excess shows that a single noise temperature does not characterize the entire dataset. This may be due to variations in weather and elevation, different observing modes, weak emission in our "off" positions, the poor spatial sampling at the edge of the OTF maps, or additional systematic errors.

5.2. *Noise characteristics*

We made a two dimensional image of the rms noise temperature, $\sigma(\mathrm{T}_A^*)$, distribution throughout the GRS (Fig. 7). We plot a histogram of the rms noise temperature versus the number of (ℓ,b) pixels with that noise temperature in Figure 8. Once again, the inset shows the same plot but on a linear rather than logarithmic scale. The rms noise temperatures were measured using the velocity region 130 to 135 $\mathrm{km\,s^{-1}}$ for Galactic longitudes $\ell \leq 40^\circ$ and from 80 to 85 $\mathrm{km\,s^{-1}}$ for Galactic longitudes $\ell > 40^\circ$ in every spectrum. We choose these velocities because they are usually emission-free toward all positions. Toward a few positions, however, Galactic emission is seen. Nevertheless, because this emission occupies a small fraction of the survey's total solid angle, it will not significantly affect the noise characteristics.

The noise distribution shows a sharp peak at $\sigma(\mathrm{T}_A^*) \sim 0.1$ K. In addition, a long tail extends to higher noise temperatures. Again, this tail shows that the observations were taken under a variety of weather conditions, elevations and observing modes. Consequently, the noise is not uniform for all positions. We find that 25% of the positions have noise temperatures < 0.08 K, 50% < 0.10 K, and 75% < 0.13 K. We will use the latter value as a typical sensitivity for the GRS. Note that this value compares well to the dispersion of the antenna temperature σ $(\mathrm{T}_A^*) = 0.12$ K for all voxels shown in Figure 6.

To compare the noise characteristics of position-switched versus OTF data we observed a small region of the survey from $40^\circ \leq \ell \leq 40\overset{\circ}{.}1$ and $-0\overset{\circ}{.}3 \leq b \leq 0^\circ$ in both modes. Figure 9 plots the noise temperature in this region for both the position-switched (dashed histogram) and OTF (solid histogram) data. The improved sensitivity of the OTF data is evident. The noise in the OTF data peaks at a $\sigma(\mathrm{T}_A^*) = 0.13\,\mathrm{K}$. The noise distribution of the position-switched data, however, peaks at a higher noise temperature of $\sigma(\mathrm{T}_A^*)$ of 0.20 K. The improvement of the OTF data over the position-switched data stems from the increased redundancy of this observing mode, which results in a larger effective integration time and reduced systematic noise sources. Figure 7 also shows these differences.

Because several "on" positions share the same "off" position, the pixel-to-pixel noise is not independent but is instead correlated. Thus, spatial averages of the data will not reduce the noise as the square root of the number of pixels. The degree to which the noise is correlated depends on the observing mode. In position-switched mode, each position is observed by only a single pixel and the array is stepped during observations such that the same array element observes four adjacent pixels for each "off" position. These pixels will therefore have correlated noise. Moreover, in the position-switched mode we step the array by multiples of the array size while mapping. Consequently, noise or gain patterns across the array will repeat on these spatial scales. Thus, we expect correlated noise at spatial frequencies corresponding to multiples of the array size. In the OTF mode, however, the array is scanned such that a single position is observed by multiple pixels. In this mode two adjacent rows share a common "off" position and correlated noise will appear at these spatial frequencies. Figures 10 and 11 show these effects.

In Figure 10, the noise images for small representative regions are shown for both OTF and position-switched modes, together with their corresponding power spectra (the square of the two-dimensional Fourier transform). As expected, the large number of faint, but sharp peaks in the power spectrum for the position-switched data correspond to the spatial frequencies of multiples of the SEQUOIA array size. In the OTF data, however, these features are essentially absent. Instead, we see a faint peak in the power spectrum at spatial frequencies corresponding to every second row.

Figure 11 shows the two power spectra of Figure 10 averaged over Galactic longitudes and latitudes. In the position-switched data correlated noise is seen in both directions because the array was stepped in both Galactic longitude and latitude. In the OTF data, however, the correlated noise due to shared "off" positions, the small peak at spatial frequencies of ~ 40 deg^{-1}, appears only in

the scan direction (Galactic latitude). Moreover, because OTF data average over several pixels the correlated noise is much smaller.

6. DATA RELEASE

The GRS data are available at www.bu.edu/galacticring. The data can be obtained either by requesting a DVD of the complete survey, or by using our on-line interface. The web page shows the Figure 1 integrated intensity image. One may access any specific FITS data cube by clicking on this image. This action selects the nearest integrated intensity image and a link to download both the corresponding FITS data cube and integrated intensity image.

For users interested in smaller regions, or particular molecular complexes, we also offer an interface to select any (ℓ,b,v) region within the survey. One can either enter the required range in Galactic longitude, Galactic latitude, and velocity, or a central position in (ℓ,b,v) and a size. Due to file size limitations, the maximum Galactic longitude range one can select is 2°. By default, the full velocity range for a given region in the survey is returned if no velocity range is entered. For input regions that overlap two data cubes, the interface will locate the relevant cubes, extract the region of interest, and generate a new cube. A link is then provided to download the FITS data cube. We also provide a link to bypass the interactive process and download individual data cubes by name. In addition, we offer several simple IDL procedures to aid users with common visualization and processing tasks.

7. SAMPLE IMAGES AND SPECTRA

The quality of GRS data can be seen in Figure 12, which shows examples of images and spectra toward five distinct regions that span a range of total molecular column density. For each region, we display a moment map and several representative spectra. The spectra typically have several velocity components, which indicate that several distinct molecular clouds lie along the line of sight.

In Figure 12(a), a region at low Galactic longitude is shown. Since the low longitudes were observed at low elevations, these data suffer from the highest system temperatures due to atmospheric extinction. Nevertheless, the moment map and spectra are not significantly compromised. Figures 12(b) and (c) show very crowded regions toward the molecular ring. Figure 12(d) is a region with relatively faint ^{13}CO emission (note that there is some faint ^{13}CO emission in the "off" beam at a $V_{LSR} \sim 12$ km s^{-1}) . Finally, Figure 12(e) shows one of the brightest star-forming regions, W51. The images reveal that the GRS has excellent dynamic range, and the spectra show that the baselines are well characterized and most of the "off" positions are emission-free.

8. SUMMARY

Using the SEQUOIA multi pixel array on the FCRAO 14 m telescope, we conducted the GRS, a new survey of Galactic ^{13}CO $J = 1 \rightarrow 0$ emission. The GRS mapped Galactic longitudes of $18° < \ell < 55.^{\circ}7$ and Galactic latitudes of $|b| < 1°$. The LSR velocity range surveyed is -5 to 135 km s^{-1} for Galactic longitudes $\ell \leq 40°$ and -5 to 85 km s^{-1} for Galactic longitudes $\ell > 40°$. The survey achieved better than half-beam angular sampling (22″ grid; 46″ angular resolution).

We have described the telescope and instrumental parameters, the observing modes, the flux calibration, the data reduction processes, and the emission and noise characteristics of the dataset. The typical sensitivity of the GRS data is $\sigma(T_A^*) \sim 0.13$ K per 0.21 km s^{-1} velocity channel. However, because the survey employed both position-switching and OTF mapping modes, and observations were conducted under a variety of weather conditions, elevations, and instrument upgrades, the noise varies across the surveyed region and thus cannot be well characterized by a single noise temperature. Since survey maps shared common "off" positions for several "on" positions, we see correlated noise at certain spatial frequencies. This correlated noise is more problematic for the position-switching data.

The GRS data are available to the community at www.bu.edu/galacticring. At this website the entire dataset can be obtained in the form of FITS data-cubes. Users can also obtain selected subsets of the data through a simple interface. The website also contains a few IDL procedures for simple, common processing tasks.

The large advance in angular sampling and sensitivity afforded by SEQUOIA on the FCRAO 14 m telescope makes the GRS an excellent new dataset for studies of molecular clouds, star forming regions, and Galactic structure.

We gratefully acknowledge observing help from Loren Anderson, Emily Flynn, Ori Fox, Dovie Holland, James Kim, Michal Kolpak, Ida Kubiszewski, Casey Law, Kristy McQuinn, Mike Martin, Courtney Morris, David Nero, Holly Naylor, Kelsy Rogers, and Todd Veach. We also wish to thank the following people at FCRAO: Peter Schloerb, Neal Erickson, Gopal Narayanan, and Michael Brewer. The GRS is a joint project of Boston University and Five College Radio Astronomy Observatory, funded by the National Science Foundation under grants AST 98-00334, AST 00-98562, AST 01-00793, AST 02-28993, and AST 05-07657.

Facilities: FCRAO.

REFERENCES

Adler, D. S., Lo, K. Y., Wright, M. C. H., Rydbeck, G., Plante, R. L., & Allen, R. J. 1992, ApJ, 392, 497
Burton, W. B. 1976, ARA&A, 14, 275
Burton, W. B., Gordon, M. A., Bania, T. M., & Lockman, F. J. 1975, ApJ, 202, 30
Clemens, D. P., Sanders, D. B., & Scoville, N. Z. 1988, ApJ, 327, 139
Dame, T. M., Hartmann, D., & Thaddeus, P. 2001, ApJ, 547, 792
Dame, T. M., Ungerechts, H., Cohen, R. S., de Geus, E. J., Grenier, I. A., May, J., Murphy, D. C., Nyman, L.-A., & Thaddeus, P. 1987, ApJ, 322, 706
Erickson, N. R., Grosslein, R. M., Erickson, R. B. & Weinreb, S. 1999, IEEE Transitions on Microwave Theory and Techniques, 47, 2212
Lee, Y., Stark, A. A., Kim, H., & Moon, D. 2001, ApJS, 136, 137
Mangum, J., Emerson, D., & Greisen, E. 2000, ASP Conf. Ser. 217: Imaging at Radio through Submillimeter Wavelengths, 217, 179
Robinson, B. J., Manchester, R. N., Whiteoak, J. B., Sanders, D. B., Scoville, N. Z., Clemens, D. P., McCutcheon, W. H., & Solomon, P. M. 1984, ApJ, 283, L31

Sanders, D. B., Clemens, D. P., Scoville, N. Z., & Solomon, P. M. 1986, ApJS, 60, 1
Scoville, N. Z. & Solomon, P. M. 1975, ApJ, 199, L105
Simon, R., Jackson, J. M., Clemens, D. P., Bania, T. M., & Heyer, M. H. 2001, ApJ, 551, 747

TABLE 1
A COMPARISON OF CO SURVEYS OF THE FIRST GALACTIC QUADRANT.

Survey	GRS	UMSB[1]	Bell Labs[2]	Columbia/CfA[3]
Dates	1998–2005	1981–1984	1978–1992	1980–
Transition ($J = 1 \rightarrow 0$)	^{13}CO	^{12}CO	^{13}CO	^{12}CO
T_R^* sensitivity per $\mathrm{km\,s^{-1}}$channel (K)	0.27	0.40	0.1	0.18
Velocity resolution ($\mathrm{km\,s^{-1}}$)	0.21	1.0	0.68	0.65
Longitude coverage (degrees)	18 to 55.7	8 to 90	−5 to 117	10 to 70
Latitude coverage (degrees)	−1 to 1	−1.05 to 1.05	−1 to 1	−6 to 6
LSR velocity range ($\mathrm{km\,s^{-1}}$)	−5 to 135	−100 to 200	−250 to 250	−140 to 140
Angular resolution (arcsec)	46	45	103	450
Angular Sampling (arcsec)	22	180	180	225–450
Number of Spectra	1,993,522	40,551	73,000	54,000
Total survey region (square degrees)	75.4	172.2	244	660

References. — (1) Sanders et al. (1986), (2) Lee et al. (2001), (3) Dame et al. (2001)

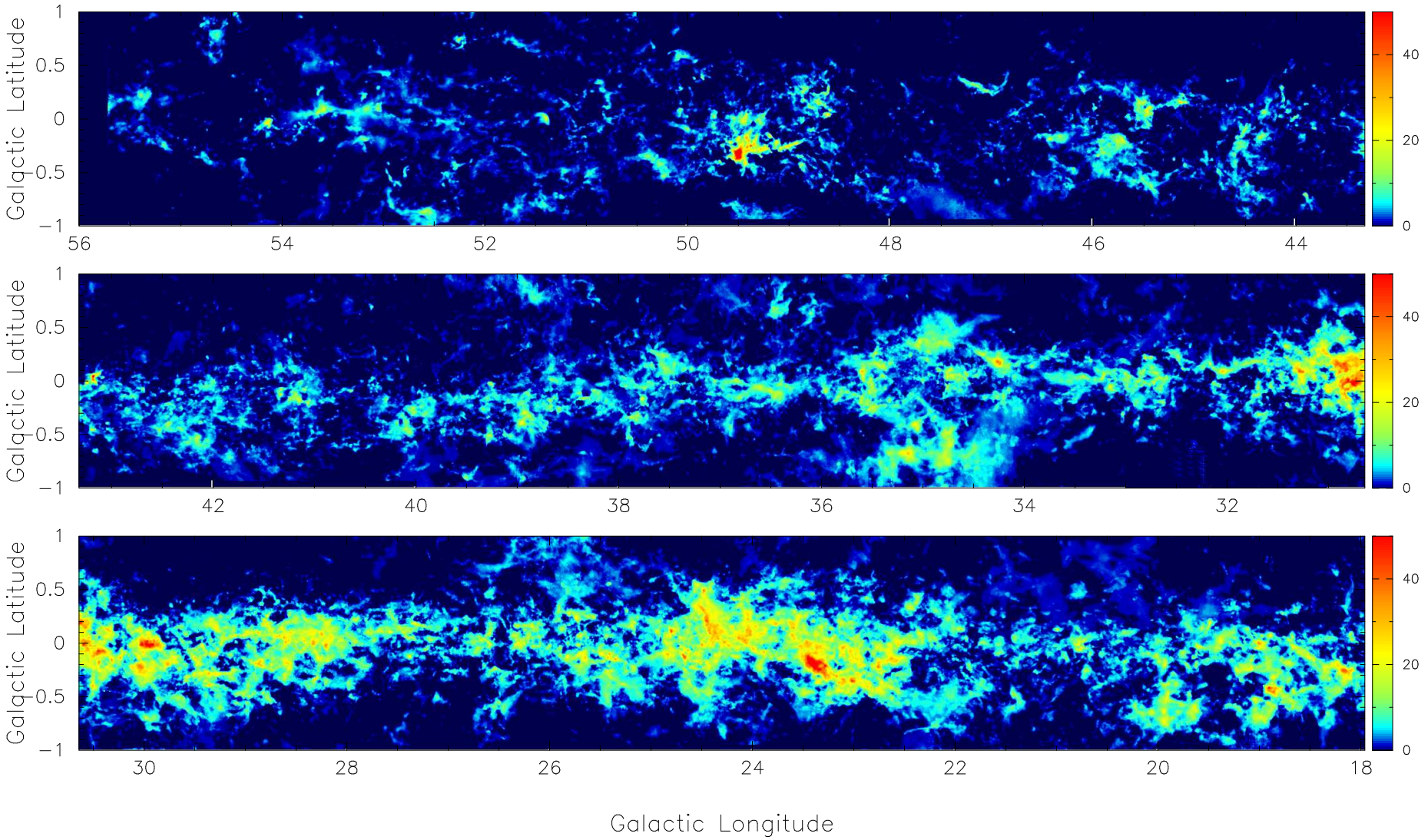

FIG. 1.— Integrated intensity image (zeroth-moment map) of GRS ^{13}CO emission integrated over all velocities (V_{LSR}= −5 to 135 km s^{-1} for Galactic longitudes $\ell \leq 40°$ and V_{LSR} = −5 to 85 km s^{-1} for Galactic longitudes $\ell > 40°$). The image shows that most of the emission is confined to $b \sim 0°$, with concentrations at $\ell \sim 23°$ and $\sim 31°$. A striking aspect of the image is the abundance of filamentary and linear structures and the complex morphology of individual clouds. The image is in units of K km s^{-1}.

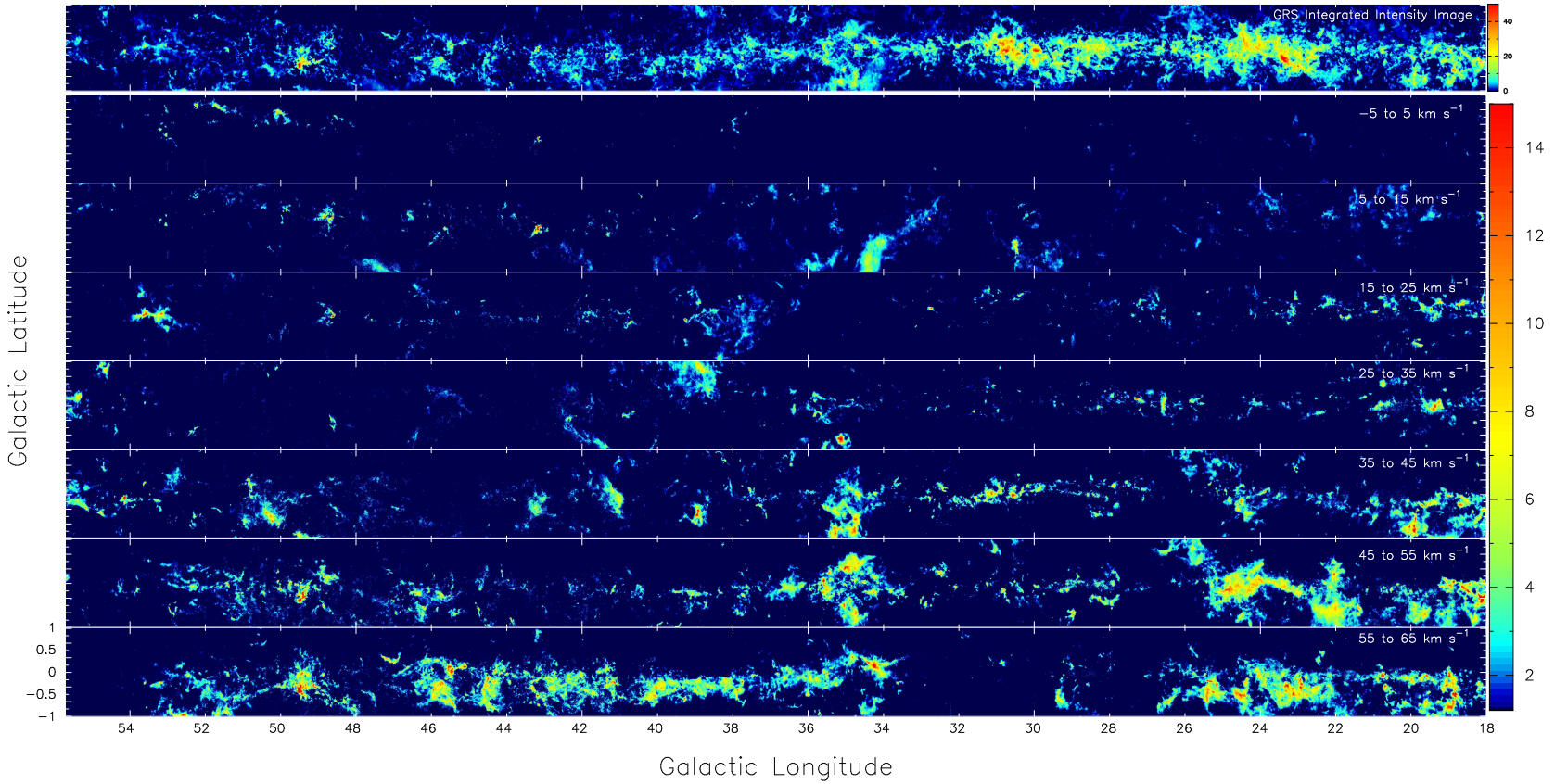

FIG. 2.— Channel maps of GRS ^{13}CO emission. The maps were made by integrating the emission over 10 km s^{-1} velocity bins. The image units are in K km s^{-1}. The top image shows the integrated intensity image from Figure 1 for comparison. The velocity range of each image is labeled. The channel maps clearly separate emission features along the same line of sight.

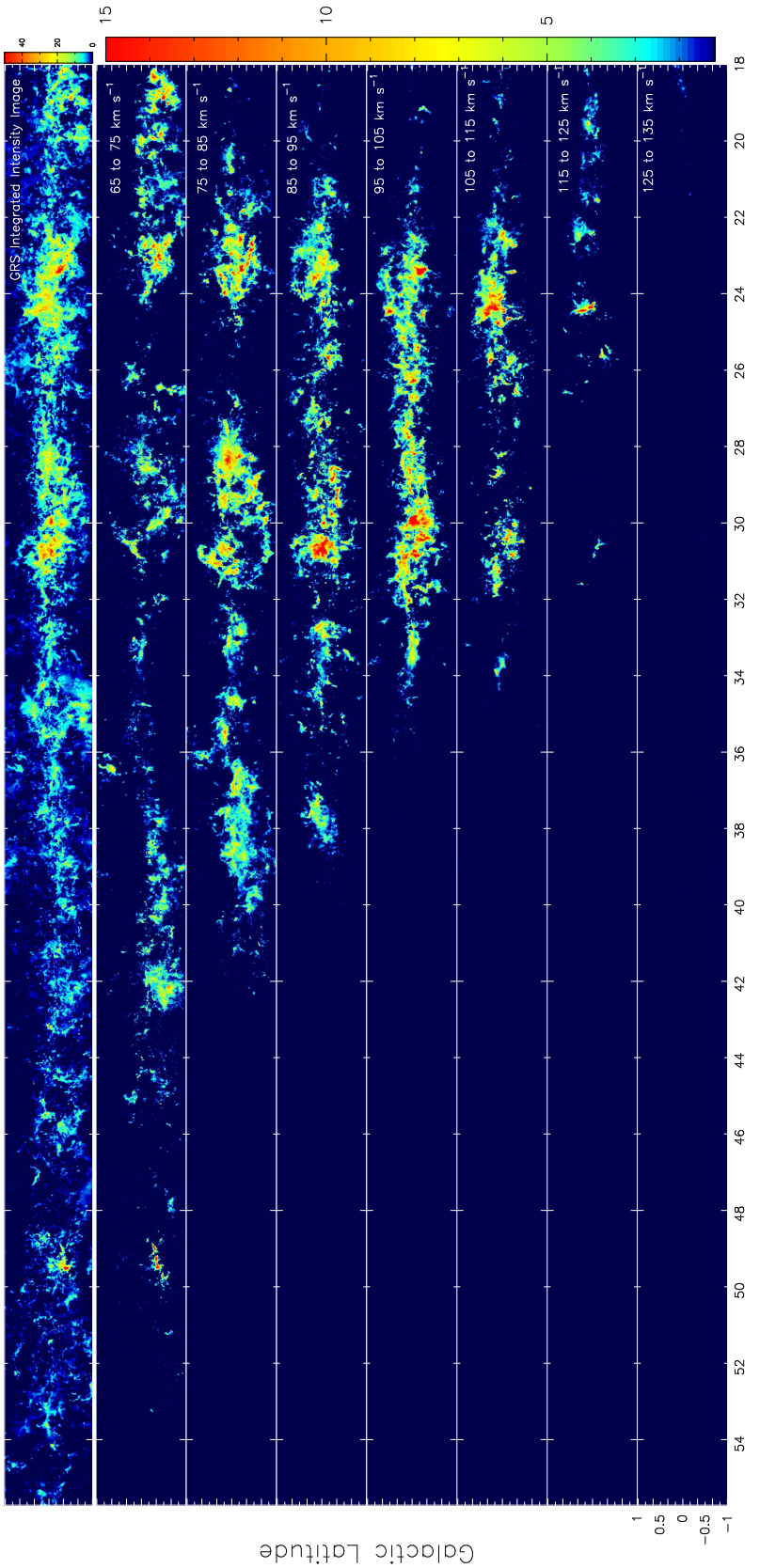

Fig. 2.– *continued*

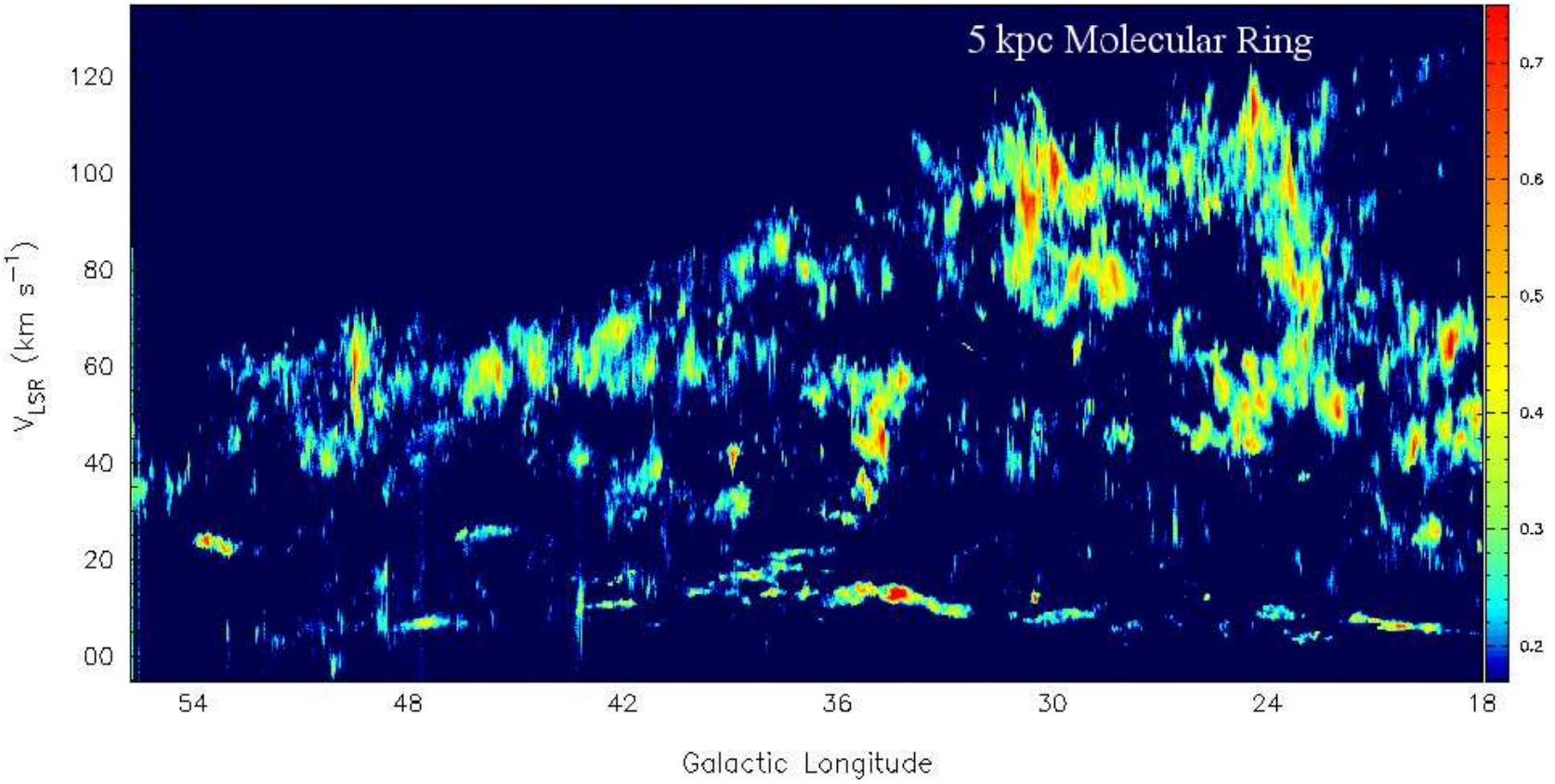

FIG. 3.— Position-velocity (ℓ-v) diagram of GRS ^{13}CO emission, made by averaging over all Galactic latitudes ($|b| < 1°$). Clearly evident are the large-scale Galactic features especially the molecular ring (the approximate location is marked). The image units are in K.

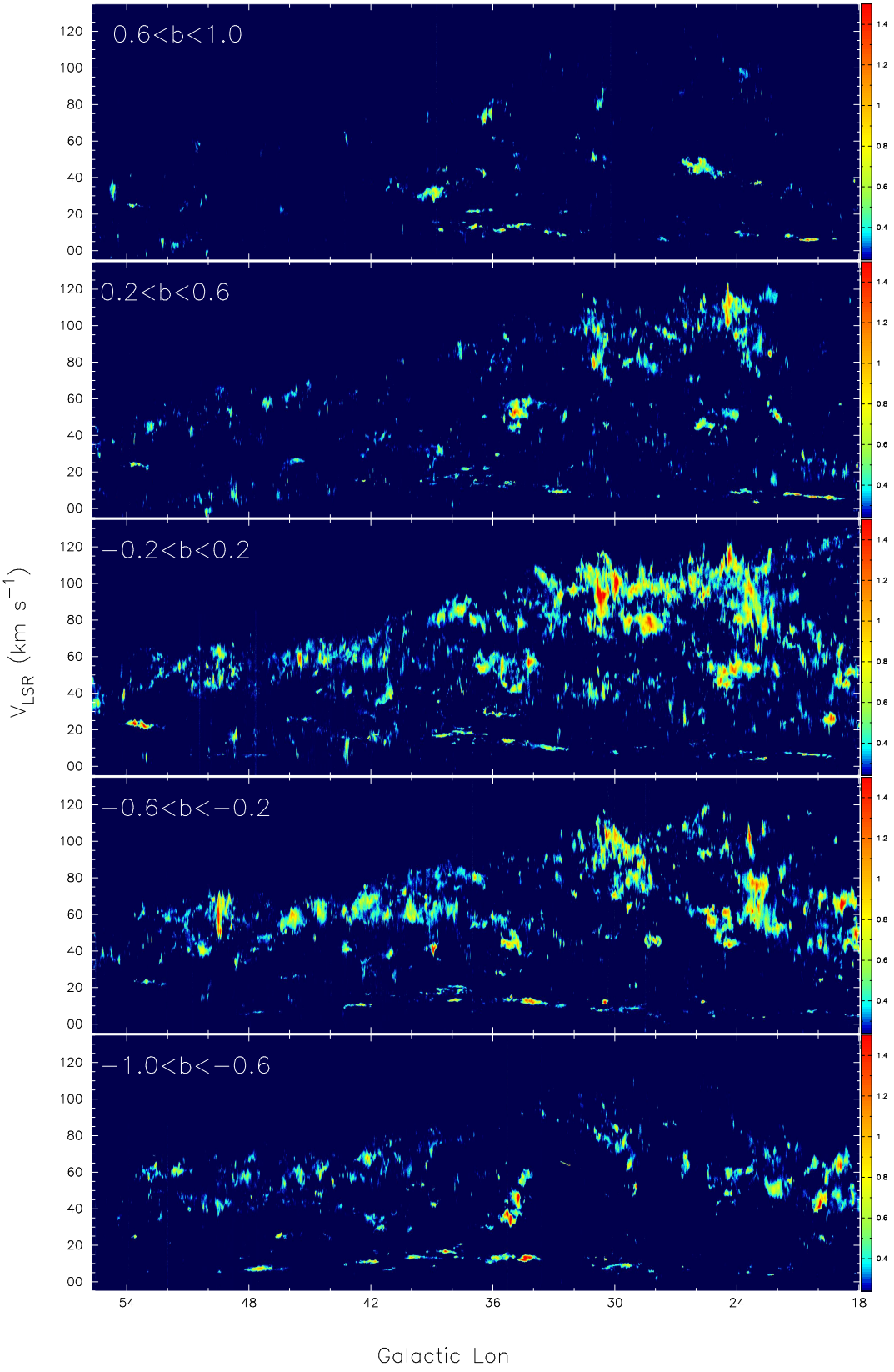

FIG. 4.— Position-velocity (ℓ-v) diagram of GRS ^{13}CO emission averaged over five ranges in Galactic latitude. The latitude coverage of each image is labeled. The image units are in K.

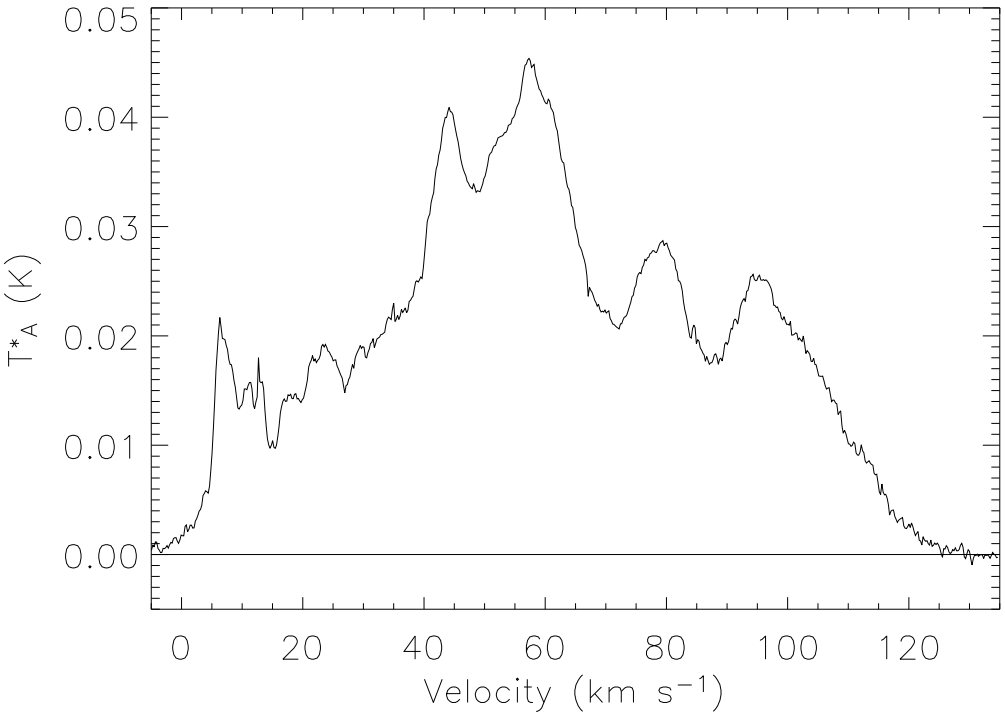

FIG. 5.— Average spectrum for the entire GRS. We see ^{13}CO emission at all positive velocities allowed by Galactic rotation, with many distinct peaks.

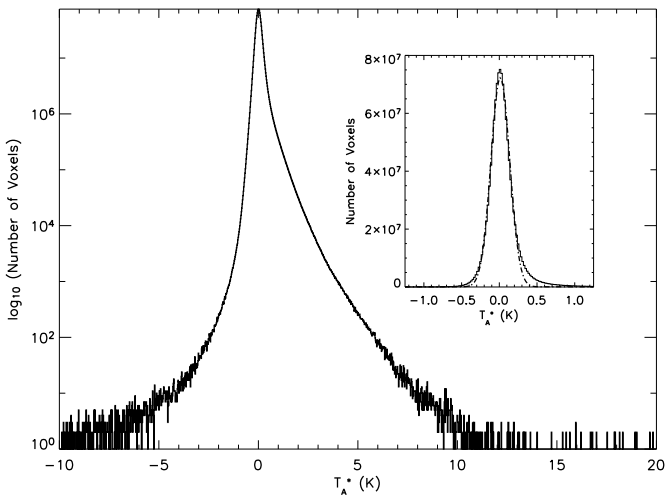

FIG. 6.— Antenna temperature distribution of all (ℓ,b,v) voxels in the GRS. The inset shows the same distribution but on a linear rather than logarithmic scale. The dash-dotted line is a Gaussian fit to the distribution (peak at 0.014 K and full-width at half-maximum of 0.29 K).

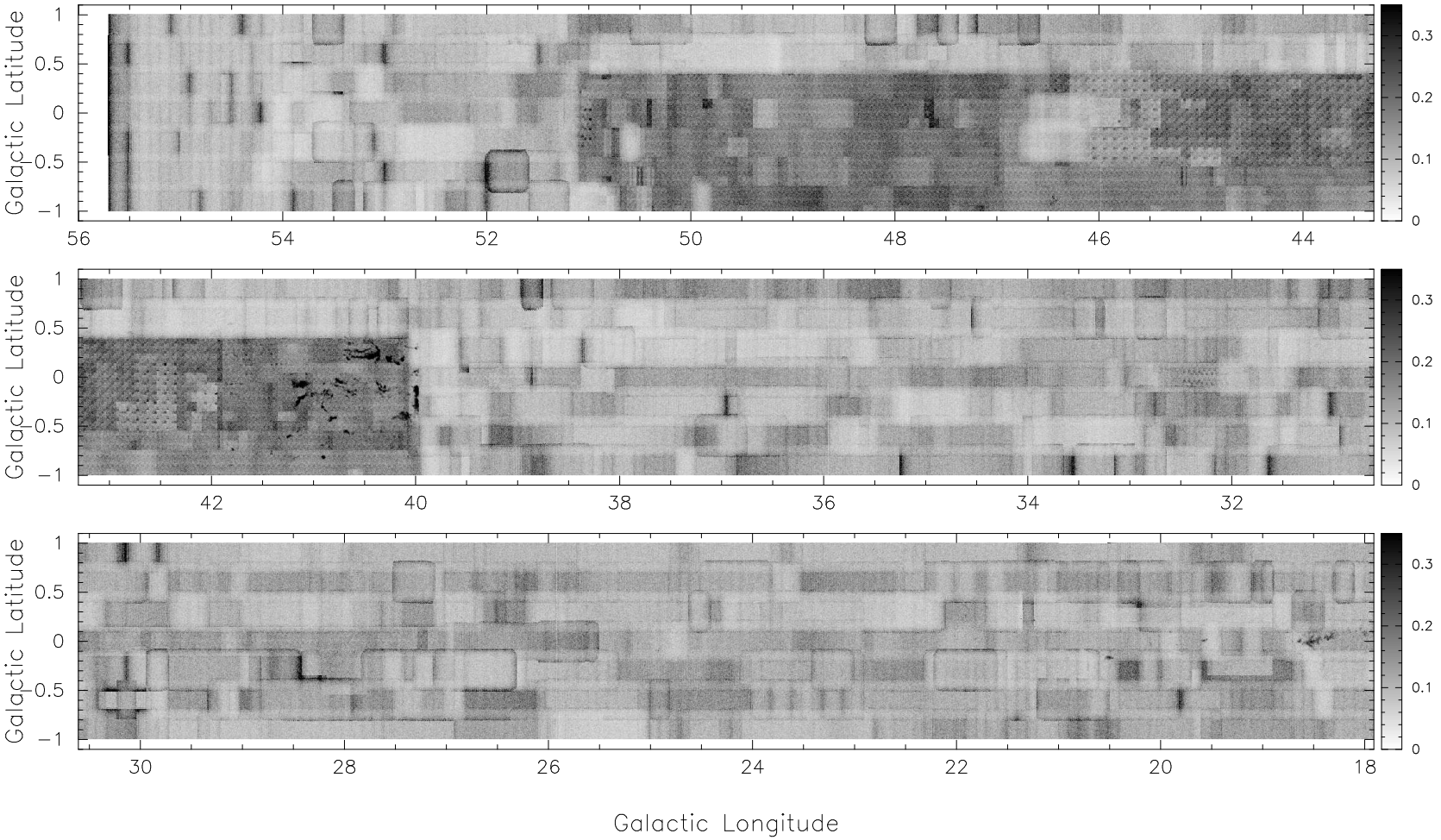

FIG. 7.— An image of the rms noise temperature, $\sigma(T_A^*)$, for the entire GRS. The image units are in K. The noise temperatures were determined using data from 130 to 135 km s^{-1} for $\ell \leq 40°$ and from 80 to 85 km s^{-1} for $\ell > 40°$. The compact features are artifacts due to emission at these velocities. The noise patterns differ for the different observing modes.

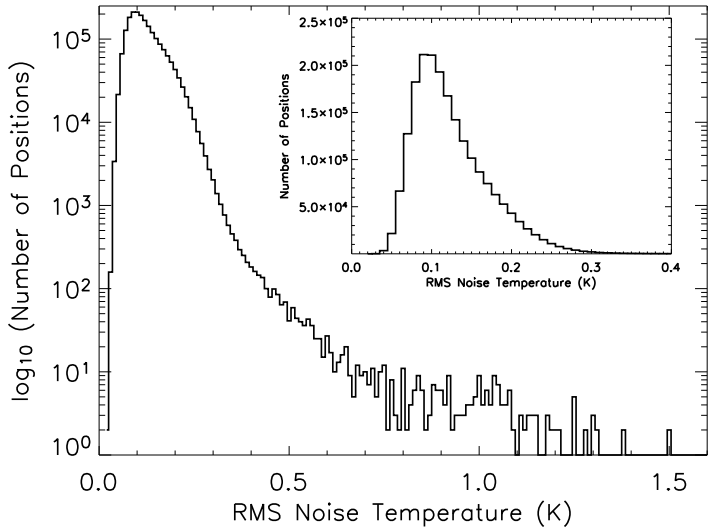

FIG. 8.— Histogram of the RMS noise temperature, $\sigma(T_A^*)$, for all (ℓ, b) positions in the GRS. The RMS noise temperatures were determined using data from 130 to 135 $\mathrm{km\,s^{-1}}$ for $\ell \leq 40°$ and from 80 to 85 $\mathrm{km\,s^{-1}}$ for $\ell > 40°$. The inset shows the same histogram but on a linear rather than logarithmic scale. The data are binned by 0.01 K intervals.

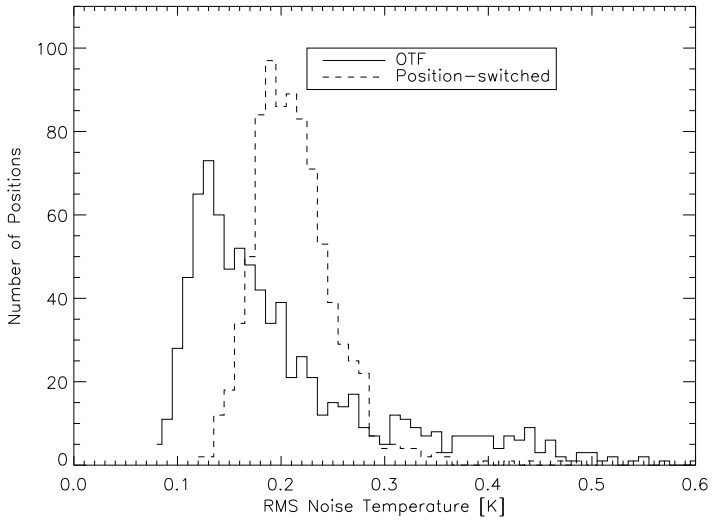

FIG. 9.— Comparison of the RMS noise temperature, $\sigma(T_A^*)$, for OTF and position-switched data. For the comparison, we use a small region of the survey ($40° \leq \ell \leq 40.^\circ 1$ and $-0.^\circ 3 \leq b \leq 0°$) that was observed in both of these modes. The improved sensitivity of the OTF data (peak at 0.13 K) compared to the position-switched data (peak at 0.20 K) is clearly evident. The data are binned by 0.01 K intervals.

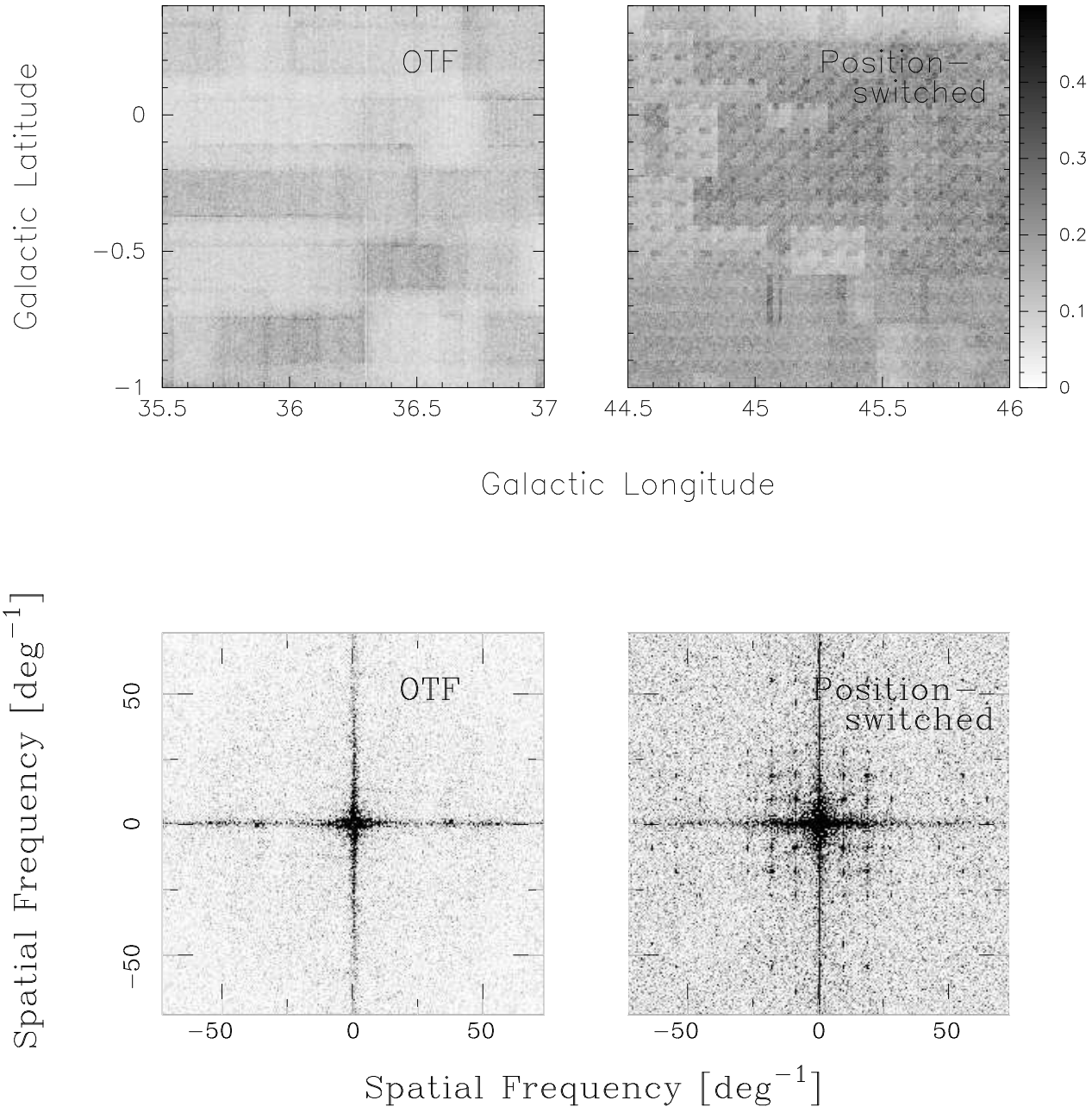

FIG. 10.— *Upper panel*: Images of the rms noise temperature for small selected regions of the GRS for the OTF (left) and position-switched modes (right). *Lower panel*: Two-dimensional power spectra of the corresponding noise images.

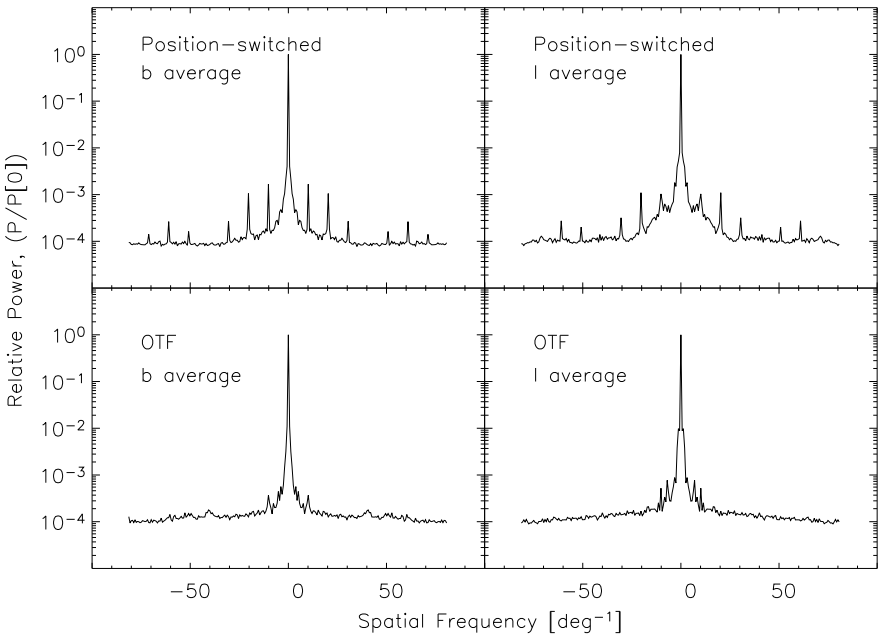

FIG. 11.— The power spectra of Figure 10 averaged over Galactic latitudes (left) and longitudes (right). Peaks in this figure represent the correlated noise at certain spatial frequencies. For the position-switched data, the peaks in both directions correspond to multiples of the array size. In contrast, the OTF data show smaller correlated noise, and also a small peak at ~ 40 deg^{-1} in the latitude plot due to the sharing of "off" positions in the scanning direction.

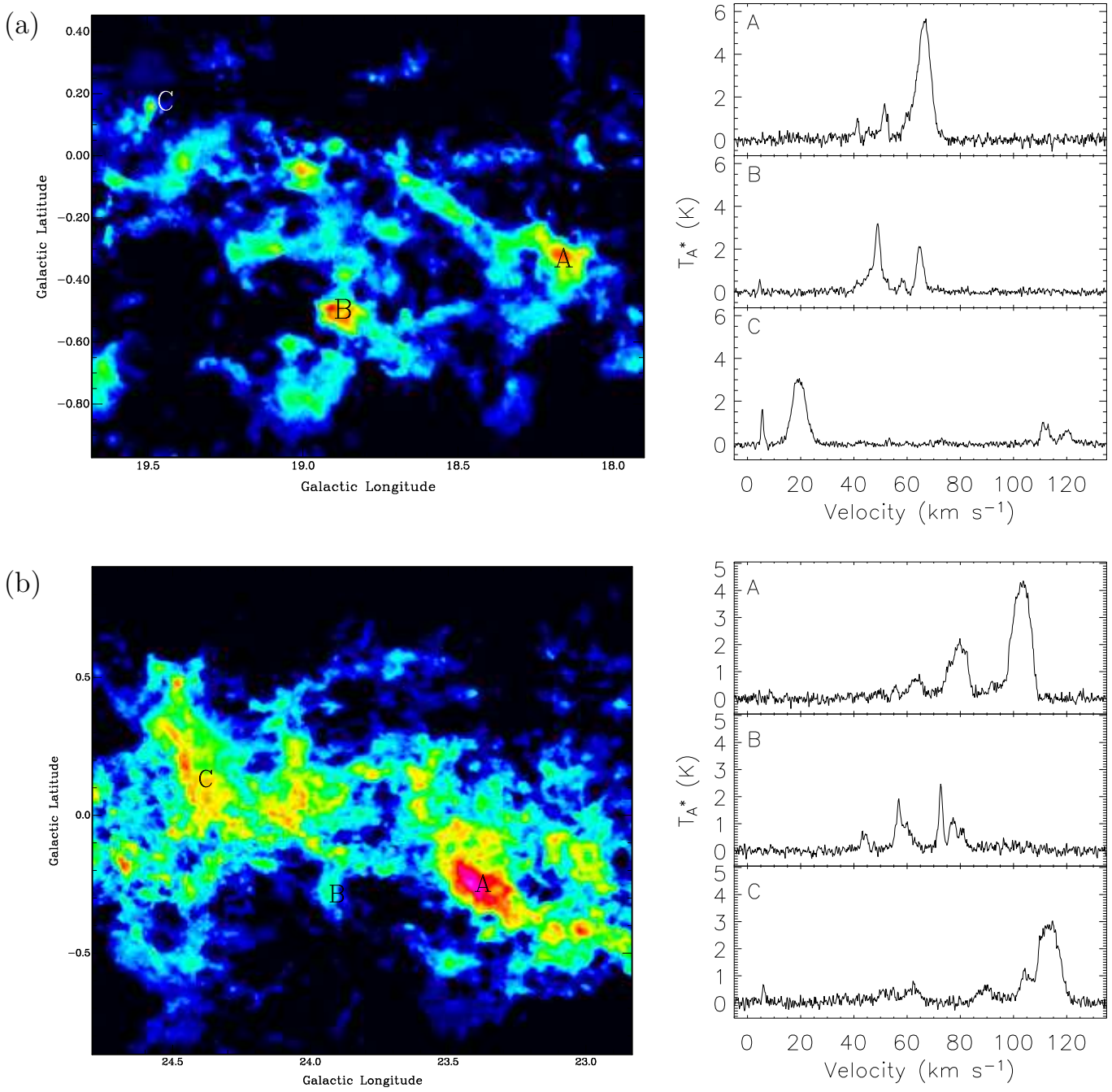

FIG. 12.— Integrated intensity images and sample spectra toward five regions within the GRS. The spectra typically show several distinct velocity components, an indication that several distinct molecular clouds lie along the line of sight. The location of each spectrum within the region is labeled on the image (A, B, and C). The transfer function is such that the following colors correspond to the following integrated intensities: black (1 K km s^{-1}), green (20 K km s^{-1}), red (45 K km s^{-1}), and white (100 K km s^{-1}).

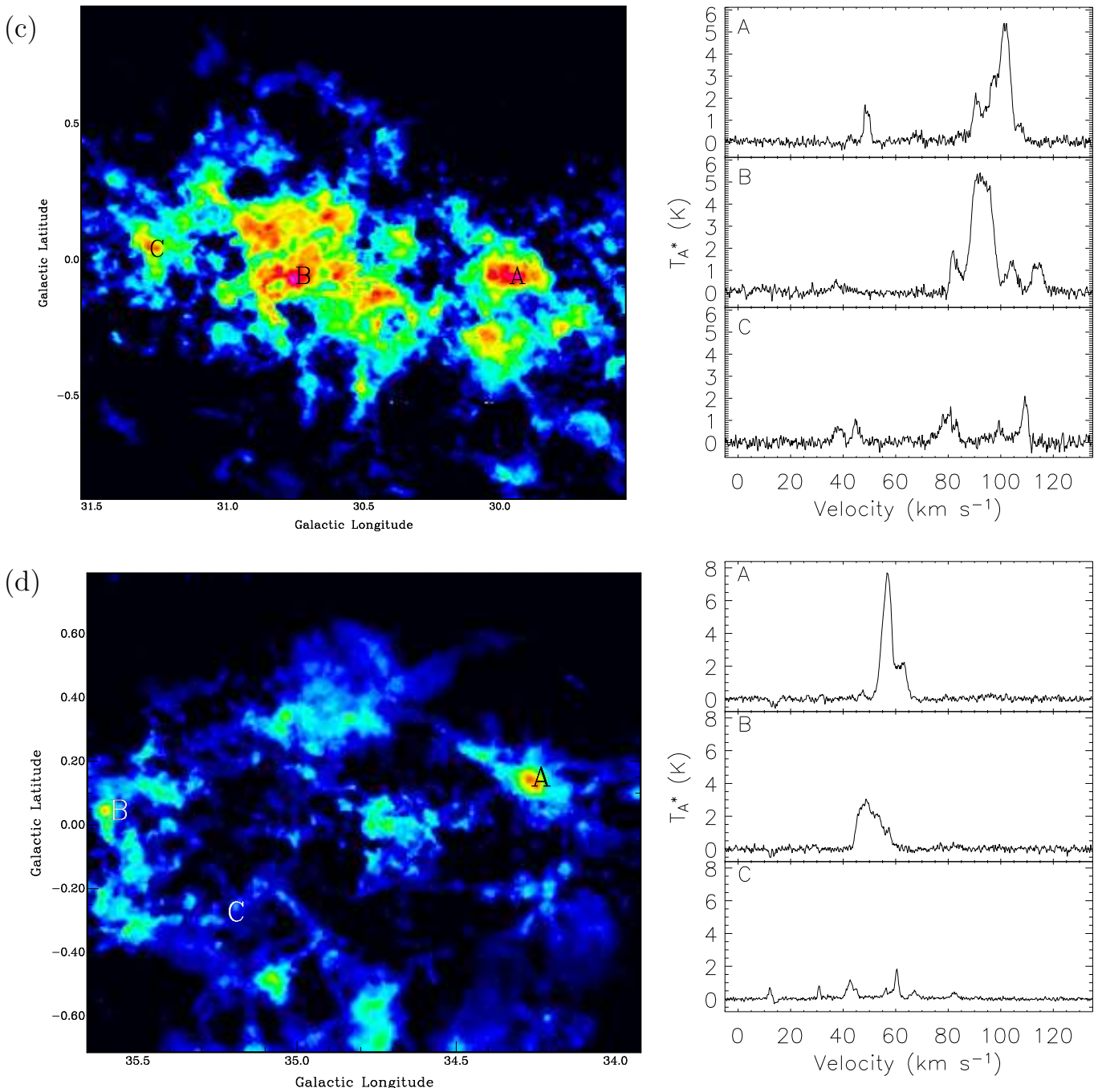

FIG. 12.– *continued*

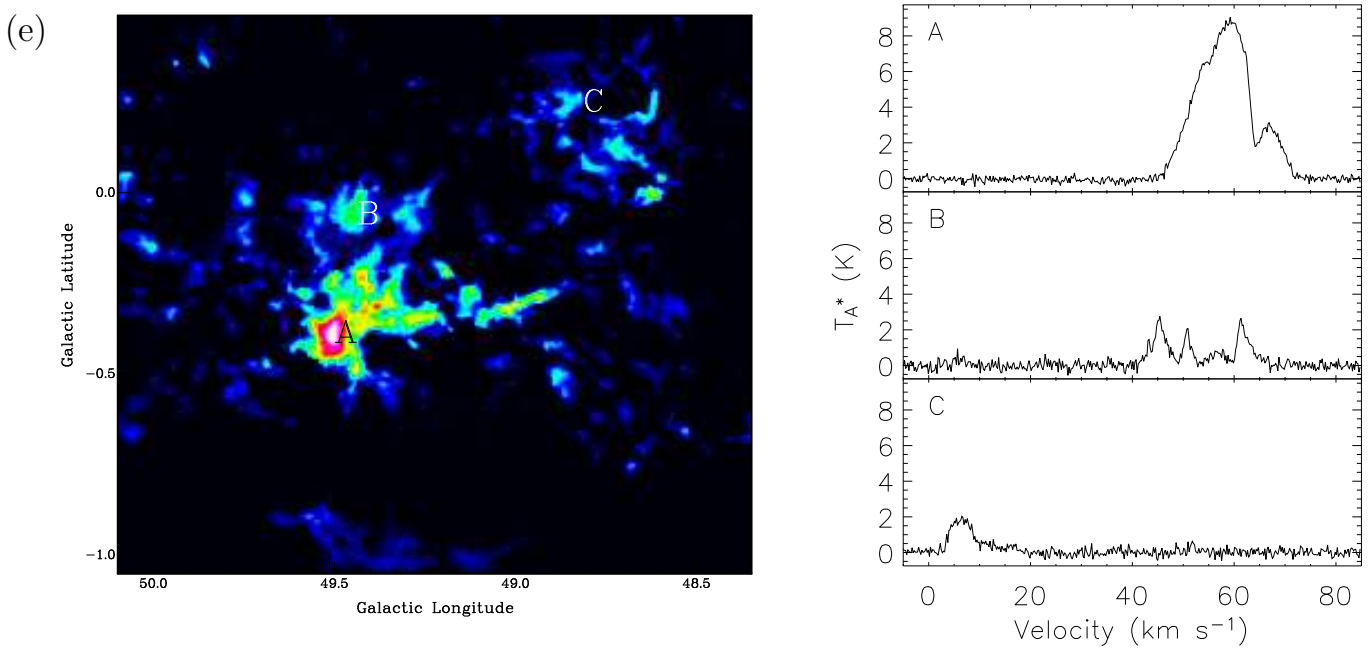

FIG. 12.– *continued*